BIOCHEMISTRY
including biophysical chemistry & molecular biology

Article

pubs.acs.org/biochemistry

The Sensitive Balance between the Fully Folded and Locally Unfolded Conformations of a Model Peroxiredoxin

Arden Perkins,[†] Kimberly J. Nelson,[‡] Jared R. Williams,[†] Derek Parsonage,[‡] Leslie B. Poole,[‡] and P. Andrew Karplus*,[†]

[†]Department of Biochemistry and Biophysics, Oregon State University, Corvallis, Oregon 97331, United States

[‡]Department of Biochemistry, Wake Forest School of Medicine, Winston-Salem, North Carolina 27157, United States

Supporting Information

ABSTRACT: To reduce peroxides, peroxiredoxins (Prxs) require a key "peroxidatic" Cys that, in a substrate-ready fully folded (FF) conformation, is oxidized to sulfenic acid and then, after a local unfolding (LU) of the active site, forms a disulfide bond with a second "resolving" Cys. For *Salmonella typhimurium* alkyl hydroperoxide reductase C (*St*AhpC) and some other Prxs, the FF structure is only known for a peroxidatic Cys→Ser variant, which may not accurately represent the wild-type enzyme. Here, we obtain the structure of authentic reduced wild-type *St*AhpC by dithiothreitol treatment of disulfide form crystals that fortuitously accommodate both the LU and FF conformations. The unique environment of one molecule in the crystal reveals a thermodynamic linkage between the folding of the active site loop and C-terminal regions, and comparisons with the Ser variant show structural and mobility differences from which we infer that the Cys→Ser mutation stabilizes the FF active site. A structure for the C165A variant (a resolving Cys to Ala mutant) in the same crystal form reveals that this mutation destabilizes the folding of the C-terminal region. These structures prove that subtle modifications to Prx structures can substantially influence enzymatic properties. We also present a simple thermodynamic framework for understanding the various mixtures of FF and LU conformations seen in these structures. On the basis of this framework, we rationalize how physiologically relevant regulatory post-translational modifications may modulate activity, and we propose a nonconventional strategy for designing selective Prx inhibitors.

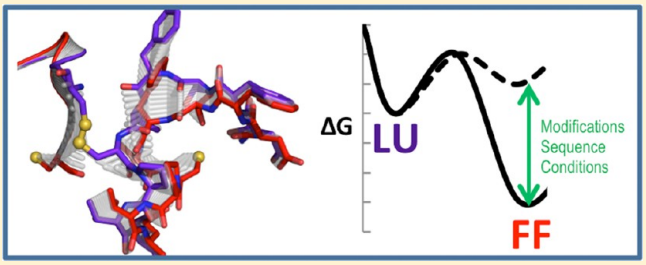

Peroxiredoxins (Prxs) are a ubiquitous family of enzymes which reduce peroxides and peroxynitrites via a reactive Cys.[1] Members of the widespread Prx1 subfamily, mostly found to form doughnut-shaped decamers, are thought to be responsible for reducing over 90% of cytosolic and mitochondrial peroxides.[1−3] The study of Prx1 enzymes also has implications for antibiotic drug design, as knockout strains of certain microbial pathogens show them to be important for surviving peroxynitrite exposure[4] (such as that generated by the host immune system[5]), for scavenging peroxide,[6] for colonization,[7] or even for growth at oxygen levels at or above 4%.[8,9] Additionally, controlled inactivation of some eukaryotic Prx1 subfamily members by a peroxide-driven hyperoxidation of the reactive Cys to a Cys sulfinate was proposed to play a role in allowing peroxide-mediated signaling.[10] The downstream oxidation of target proteins by locally accumulated hydrogen peroxide is increasingly recognized as important in many such signaling pathways,[11] with particularly well-studied examples being the inhibition of protein Tyr phosphatases via oxidation of an active site Cys.[11−15] Physiologically relevant regulation of Prx1 enzymes is also thought to occur by phosphorylation,[11,13,16,17] Lys acetylation,[18] glutathionylation,[19] and proteolysis.[11,20]

Structural studies have shed much light on the mechanism of the Prx1 family of Prx enzymes (also called typical 2-Cys Prxs). For these enzymes, key residues are a peroxidatic Cys, termed C_P, contained within an absolutely conserved PXXX(T/S)XXC motif, an additional conserved Arg, and a resolving Cys, termed C_R, located near the C-terminus[1,21] (Figure 1a). The basic active unit involves a so-called "B-type" homodimer with two active sites, each involving the C_P from one subunit and the C_R from the other (Figure 1a), with the association of five such dimers at "A-type" interfaces building the toroidal $(\alpha_2)_5$ decamer (Figure 1b).[22] The active site stabilizes the C_P thiolate ($pK_a \approx 6.0$)[23] as well as specifically binding and activating the peroxide substrate.[1,24] In the catalytic cycle (Figure 1c), an S_N2 nucleophilic attack of the C_P thiolate on the peroxide substrate forms a C_P-sulfenic acid and water (or corresponding alcohol); the C_P-sulfenic acid is then attacked by C_R to form an interchain C_P—C_R disulfide (and another molecule of water) which is in turn reduced, most commonly by a thioredoxin-type protein.[1,21,24]

Received: August 22, 2013
Revised: October 18, 2013
Published: October 31, 2013

dx.doi.org/10.1021/bi4011573 | *Biochemistry* 2013, 52, 8708−8721

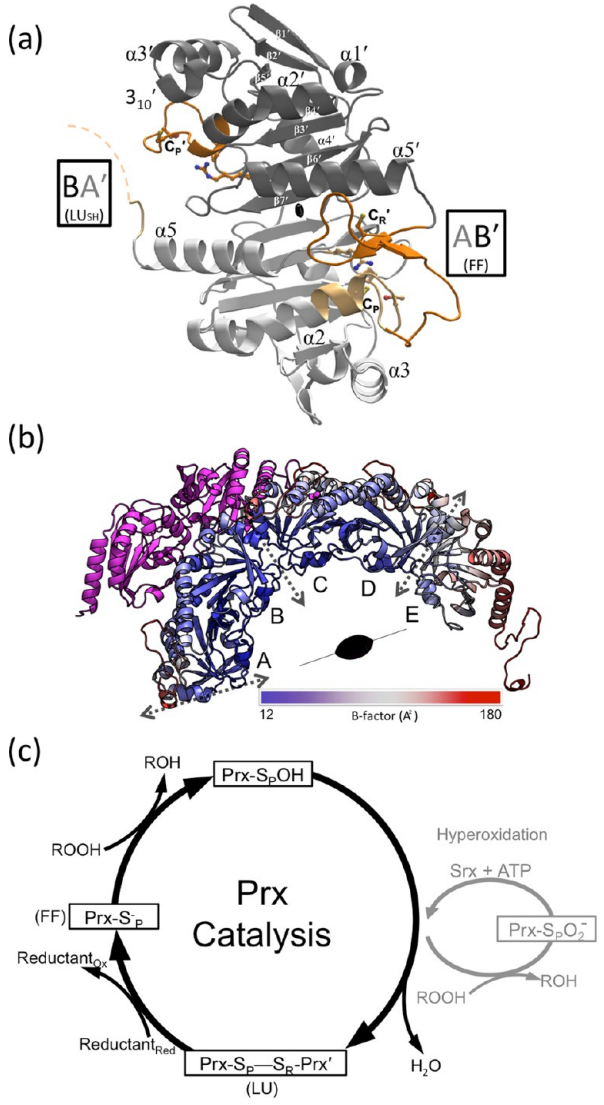

Figure 1. Structure and catalysis of *St*AhpC. (a) A B-type dimer unit of *St*AhpC with the key catalytic residues depicted as sticks, and select Prxs fold core elements of seven β-strands and five helices[22] labeled. Chains A (light gray/light orange) and B (dark gray/dark orange) from the WT_{DTT} structure illustrate the FF AB′ active site and the LU_{SH} BA′ active site (seen at ~50% occupancy). The active site loop (residues 40−50) and C-terminal (residues 161−186) regions are highlighted (orange tones), as is the disordered BA′ C-terminal region (dashed curve). (b) The half-decamer observed in the *St*AhpC WT_{DTT} asymmetric unit is colored according to mobility from low (blue) to high (red) as indicated. Decamer-building interfaces between B-type dimers (dotted gray two-headed arrows) and the crystallographic 2-fold axis that generates the decamer are indicated. Also shown is the symmetry mate hindering folding of the chain A C-terminus (magenta). (c) The Prx catalytic cycle (black) and the hyperoxidation regulatory shunt active in some eukaryotes (gray) are shown. FF and LU conformations involved in catalysis are indicated.

In the enzyme form that reacts with peroxide, C_P and C_R are ~14 Å apart, and C_R is buried; therefore, the formation of the C_P—C_R disulfide requires a substantial local unfolding of both the active site loop (i.e., residues ~40−50, which contain C_P) of one chain and the C-terminus (containing C_R) of its partner chain in the homodimer. Each active site of these enzymes, therefore, has at least two discrete conformations relevant to the catalytic cycle (Figure 1): (1) an FF conformation, with a substrate-ready active site pocket, and (2) an LU conformation having the active site loop rearranged and the C-terminal residues beyond C_R disordered.[1,25] This FF↔LU transition is not only important for catalysis, but it has been shown to be the main factor governing the sensitivity of Prx1 subfamily enzymes to hyperoxidative inactivation.[10] Some remaining points of uncertainty are, however, the extent to which the unfolding of the active site loop and C-terminus are coordinated, how the conformational equilibrium is altered by modifications, and whether the catalytic states of C_P-SH and C_P-SOH are locked into a certain conformation or are dynamically transitioning between them. NMR and crystallographic evidences imply that there is a preexisting dynamic equilibrium for the C_P-SH form for a monomeric plant enzyme in the PrxQ subfamily,[25,26] while one human Prx1 subfamily enzyme has recently been reported to specifically convert to the LU conformation when in the C_P-SOH form.[27]

We address these questions here using *Salmonella typhimurium* alkyl hydroperoxide reductase C (*St*AhpC), one of the first discovered Prxs and a model system for studying Prx1 catalysis,[28,29] oligomerization,[22] and regulation.[10] Among the six *St*AhpC crystal structures reported, four exhibit the LU disulfide conformation (LU_{S-S})—with one wild type[22] and four mutants[29,23]—while only one, a C_P→Ser (i.e., C46S) mutant, adopts the FF conformation.[10] We speculated that the *St*AhpC C46S mutant structure may not accurately represent the properties of the reduced wild-type enzyme and thus sought to obtain a structure of the authentic wild-type FF active site. Here, we report that soaking the LU_{S-S}-form crystals in 1,4-dithiothreitol (DTT) provides a structure of FF wild-type *St*AhpC (FF_{WT}) in a crystal environment that can accommodate both the FF and LU conformations. In addition, we developed a protocol to crystallize the C_R→Ala mutant in the same crystal form. This allows for a rare level of insight not only into the conformational, dynamic, and thermodynamic aspects of the FF↔LU equilibrium that is essential to Prx function, but also into the influences C_P→Ser and C_R→Ala mutations have on those aspects of that equilibrium.

EXPERIMENTAL PROCEDURES

Crystallography. *C165A Creation and Purification of Wild-Type and Mutant AhpC Proteins.* The C165A mutation of *St*AhpC was created using the QuikChange site-directed mutagenesis kit (Stratagene) and validated by sequencing the entire gene. Wild-type and mutant *St*AhpC were expressed from the pTHCm-*ahpC* vector[23] in JW0598 (lacking *ahpC*) *E. coli* cells[30] grown in Studier's ZYM-5052 autoinduction media.[31] The purification procedure for all AhpC mutant proteins was essentially the same as described previously[32] except that 10 mM β-mercaptoethanol (BME) was included in all buffers used during the purification of C165A to prevent hyperoxidation of the C_P. After purification by phenyl sepharose and ion exchange chromatography, the C165A protein was concentrated and exchanged into 25 mM potassium phosphate, pH 7.0, 1 mM ethylenediaminetetraacetic acid (EDTA), and 2 mM DTT. As seen from the results, apparently some BME remained present after the buffer exchange. The concentration of AhpC was determined by absorbance at 280 nm with ε = 24 300 M^{-1} cm^{-1}.[32]

Crystallization of Wild-Type StAhpC and C165A Mutant. Initial crystallization was essentially as described by Wood et al.[22] For the wild type, optimal crystals were grown at 300 K in hanging drops formed by 4 μL of 14.3 mg/mL protein (in 25

dx.doi.org/10.1021/bi4011573 | *Biochemistry* 2013, 52, 8708−8721

Table 1. Data Collection and Refinement Statistics

data collection	PDB code: 4ma9	PDB code: 4mab
structure	WT_{DTT}	$C165A_{DTT}$
space group	$C222_1$	$C222_1$
unit cell *a*, *b*, *c* (Å)	126.81, 171.13, 135.34	127.23, 172.42, 136.21
resolution (Å)	36.8−1.82 (1.92−1.82)[a]	29.2−1.90 (2.00−1.90)
completeness (%)	96.7 (91.1)	100.0 (100.0)
unique reflections	126 642 (17 246)	117 456 (17 015)
multiplicity	13.0 (12.7)	6.8 (6.4)
R_{meas} (%)	23.1[b] (408)	23.8[c] (1048)
$\langle I/\sigma \rangle$	10.6 (0.6)[d]	6.2 (0.2)[e]
$CC_{1/2}$	1.00 (0.16)	0.995 (0.20)
Refinement		
resolution range (Å)	36.7−1.82	29.2−1.90
R-factor (%)	20.4	19.8
R_{free} (%)	24.0	23.9
molecules in AU	5	5
protein residues	907	909
water molecules	518	232
total atoms	14 776	14 454
rmsd[f] lengths (Å)	0.012	0.016
rmsd angles (deg)	1.3	1.6
Ramachandran plot[g]		
φ, ψ-preferred (%)	97.6	97.2
φ, ψ-allowed (%)	2.4	2.7
φ, ψ-outliers (%)	0.0	0.1[h]
B-factors	1 TLS group/monomer	1 TLS group/monomer
<main chain> (Å^2)	48	56
<side chains and waters> (Å^2)	59	64

[a]Values in parentheses are for the highest-resolution shell; preceding values are for all data. [b]R_{meas} in the inner shell (40−5.76 Å) is 3.3%. [c]R_{meas} in the inner shell (30−6.01 Å) is 3.8%. [d]$\langle I/\sigma \rangle$ of the inner shell is 58.1 and falls to ∼2 at 2.15 Å. [e]$\langle I/\sigma \rangle$ of the inner shell is 30.8 and falls to ∼2 at 2.30 Å. [f]rmsd = root-mean-square deviation. [g]Preferred, allowed, and outlier angles as assigned by Molprobity.[66] [h]V164 chain A has weak density but is near an allowed region.

mM phosphate-buffered saline (PBS), 1 mM EDTA, pH 7.0) mixed with 1 μL of artificial mother liquor (AML) containing 1.4 M $MgSO_4$ and 0.1 M 2-(*N*-morpholino)ethanesulfonic acid (MES) at pH 6.5. Microseeding produced larger and better-diffracting crystals. Briefly, the initial crystals were crushed in 100 μL of AML and vortexed, and a serial dilution of seed stock concentrations was created. Drops were seeded by dipping a 21-gauge needle into the seed stock and then streaking it across the new drop. Large, tapering column crystals on the order of ∼0.5 mm grew in 1−14 days. As expected, these crystals contained protein in the disulfide form, and for reduction, the crystals were soaked for 2 min in freshly prepared AML containing 0.1 M DTT (Figure S1 of the Supporting Information). Some stress lines did appear on the crystals when this soak was performed.

Many attempts to grow $C222_1$ crystals of untreated C165A produced only a single crystal that grew after more than a month. Peroxide at 100 mM was added to some crystallization trials to attempt to produce homogeneous oxidized protein, and crystals grew much more readily. Analysis of the treated protein by mass spectrometry showed that the predominant redox states of the enzyme were C_P-SO_3^- and a form with the molecular weight expected for a BME adduct that presumably was produced by residual BME from the purification reacting with transiently formed C_P-SOH (Figure S2 of the Supporting Information). These crystals yielded a structure that was 100% LU but, when soaked with DTT, a portion of the enzyme shifted to the FF conformation. We inferred that the portion of the protein forming the BME adduct was being reduced and shifting its conformation to FF, and the portion containing C_P-SO_3^- was not being reduced and was remaining in the LU conformation. Though not conclusive, this observation implies that the C_P-SO_3^- form of *St*AhpC behaves differently than two other Prxs for which this form was shown to be FF.[33,34] In refining the protocol to produce maximal C165A−BME adduct with minimal C_P-SO_2^-/SO_3^- formation, we settled on the addition of 10 μM BME and 20 μM peroxide, on the basis of trials of several concentrations that were analyzed with mass spectrometry (Figure S2 of the Supporting Information). In our final protocol, crystals of C165A were obtained by seeding with crushed wild-type LU_{S-S} crystals in drops that were first treated with 10 μM BME for 30 min, with the subsequent addition of hydrogen peroxide to give a final concentration of 20 μM. A DTT soak of these crystals was carried out as for wild-type *St*AhpC. Here, we refer to the DTT-soaked structures of the wild type and C165A as WT_{DTT} and $C165A_{DTT}$, respectively.

For freezing both the wild type and C165A crystals, glycerol was added to the drop as a cryoprotectant to make a final concentration of ∼20%. Because the crystals dissolved if the glycerol was added too quickly, the glycerol was placed beside the crystal drop, a small channel was created between them with a pipet tip, and they were allowed to equilibrate for ∼2 min. The crystals were then scooped and frozen by plunging them into liquid nitrogen.

Data Collection. Data were collected at the Advanced Light Source (ALS) Lawrence Berkeley National Laboratory beam-

dx.doi.org/10.1021/bi4011573 | *Biochemistry* 2013, 52, 8708−8721

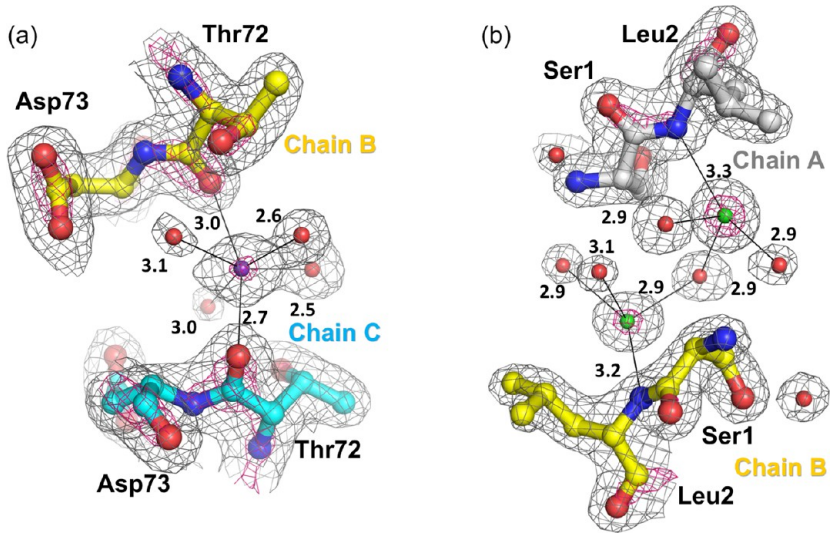

Figure 2. Evidence for bound ions at subunit interfaces in the WT_{DTT} structure. (a) Representative of all decamer-building interfaces, a potassium (purple sphere) is coordinated by Thr72-O of chains B and C and four water sites (red spheres). The $2F_O$-F_C density is contoured at 1.5 ρ_{rms} (root mean square electron density; gray mesh) and 5.0 ρ_{rms} (hot pink mesh), and coordinating interactions (black thin bonds; distances in Å) are shown. Evidences for the assignment are the strong electron density, the roughly octahedral coordination with distances near 2.8 Å as is uniquely expected for a potassium,[67] and the presence of 25 mM potassium phosphate in the protein buffer. If modeled as a water, strong difference density appears. This site is incorrectly modeled as a water in previous *St*AhpC structures. (b) Representative of all dimer interfaces, chloride ions (green spheres) modeled near the positively charged α-amino group of chains A and B. The $2F_O$-F_C density is contoured at 2.0 ρ_{rms} (gray mesh) and 6.0 ρ_{rms} (hot pink mesh). When modeled as a water, strong difference density is observed. These ions are also present in the $C165A_{DTT}$ structure but do not appear to be present in C46S *St*AhpC crystals.

lines 5.0.2. and 8.2.2. The data were indexed and integrated with Mosflm version 7.0.9.[35] All crystals of *St*AhpC were found to be in the space group $C222_1$ and exhibited similar unit cell dimensions as previous *St*AhpC structures, with $a \approx 127$ Å, $b \approx 171$ Å, and $c \approx 135$ Å (see Table 1). The resolution cutoff criterion was based on the new statistic $CC_{1/2}$, recently introduced by Karplus and Diederichs,[36] which demonstrated that better models are obtained when resolution is extended to the $CC_{1/2}$ = 0.1−0.2 range despite the fact that R_{meas} values become disturbingly large and $\langle I/\sigma \rangle$ unconventionally low. We have applied this new criteria in recent studies and discussed its value,[25,37] and we note that a recent detailed study by Evans and Murshudov[38] concluded that useful signal is contained in data out to the $CC_{1/2}$ ~0.2−4 range and "it seems sensible to set a generous limit so as not to exclude data containing real (if weak) information." For our structures, we implemented a cutoff of $CC_{1/2}$ ~0.2 in the highest resolution shell (Table 1) and obtained improved maps. The effective resolution of a structure is difficult to define, but for comparison with past structures, we also note the resolution at which $\langle I/\sigma \rangle \approx 2$ (Table 1). R_{free} flags were randomly assigned to 5% of the WT_{DTT} data set, and the same flags were imported to use for the $C165A_{DTT}$ data set.

Refinement of DTT-Soaked Structures. An initial model for WT_{DTT} was constructed on the basis of the *St*AhpC C46S crystal structure (PDB entry 1n8j of spacegroup *P*1)[10], with active site residues 40−50 and 161−186 removed to produce maps that were unbiased for these regions. Chains K, L, O, P, and R of 1n8j were superimposed on the half-decamer of PDB entry 1yep, one of the previously solved LU $C222_1$ *St*AhpC structures,[22] and this model was refined using BUSTER,[39] producing initial R/R_{free} values of 25.0%/28.9%. All chains were found to have had their disulfides reduced, and the active sites were modeled as FF or LU with no disulfide formed (LU_{SH}) or LU with only the C-terminal region unfolded ($LU_{C\text{-}term}$), based on omit map density. Coot[40] was used to perform manual rebuilding, with main initial changes including the addition of solvent molecules and adjustment of some side-chain rotamers. No noncrystallographic-symmetry (NCS) restraints were used. End-stage refinements were performed with PHENIX.[41] Adding riding hydrogens reduced R_{free} by ~0.5%, and using translation-libration-screw (TLS) refinement with one group per protein chain reduced the R_{free} by ~3%. The occupancy of the chain B active site loop was estimated to be ~0.5:0.5 FF:LU. We expect that remaining positive difference density in this region is due to solvent molecules that coordinate with Arg119 when the active site is LU, as was observed in the LU_{S-S} structure.[22] On the basis of evidence (see Figure 2 legend), residual positive difference map peaks at sites that had been modeled as waters were replaced by potassium and chloride ions and six glycerol molecules. There remains one fairly large and oddly shaped difference density feature at each decamer-building interface, which we were not able to interpret (Figure S3 of the Supporting Information). The WT_{DTT} final R/R_{free} was 20.4%/24.0%, and the final refinement statistics are reported in Table 1.

Refinement for $C165A_{DTT}$ utilized the final WT_{DTT} model as a starting model with active site residues 40−50 and 160−186 removed (initial R/R_{free} = 24.4%/26.4%). As for WT_{DTT}, the chain B active site loop was modeled as 50:50 $LU_{SH}/LU_{C\text{-}term}$. Residues 40−50 of chains A, C, D, and E were modeled only as fully occupied FF, despite residual low-level density that could be due to some LU population; the C-terminal regions were modeled as partially occupied FF on the basis of consistent $2F_O$-F_C and F_O-F_C density for the expected FF chain path. Test refinements varying the occupancy in increments of 0.1 gave 0.6 as the occupancy at which the *B* factors for this region were closest to those observed for the WT_{DTT} structure. A residual difference peak near the position occupied by wild-type Cys165-Sγ was left uninterpreted, and we suspect it is due to

dx.doi.org/10.1021/bi4011573 | *Biochemistry* 2013, 52, 8708−8721

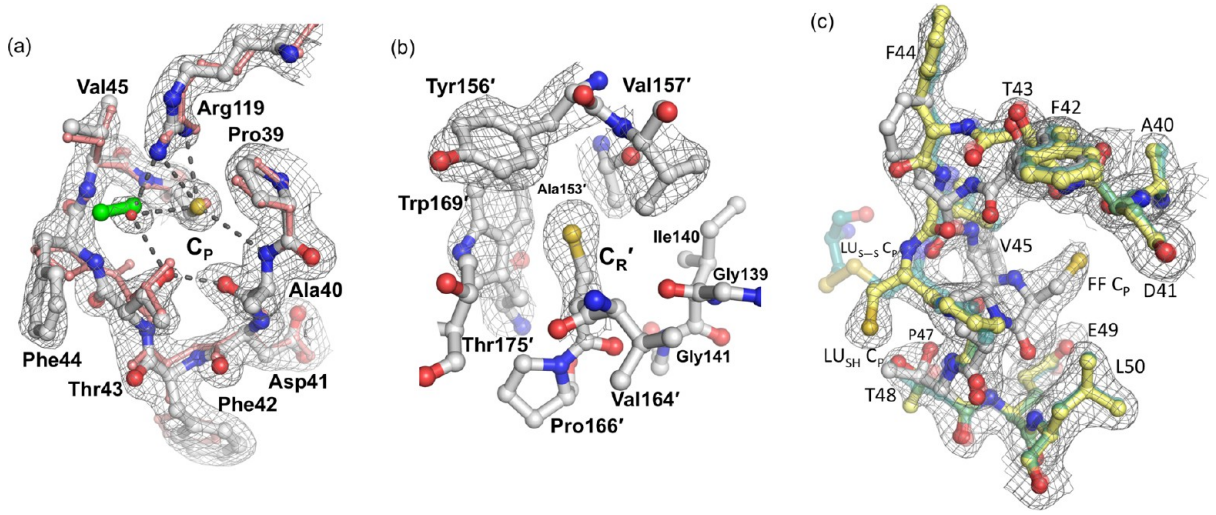

Figure 3. The WT_{DTT} C_P and C_R environments in FF chains. (a) The FF active site loop of wild-type *St*AhpC chain A (white) in $2F_O$-F_C electron density (gray mesh contoured at 1.5 ρ_{rms}) matches the conformation of peroxide-bound *Ap*Tpx (pink protein and green peroxide; PDB code 3a2v). Selected polar interactions are indicated by dashed lines. In *St*AhpC, a bound water (red sphere) overlays with the position of the *Ap*Tpx hydrogen peroxide substrate. (b) The FF C_R environment in chain B (white) is shown with $2F_O$-F_C electron density (contoured at 1.0 ρ_{rms}). The FF C_R is buried in a pocket formed by Ile140, Tyr156′, Val157′, Trp169′, and Thr175′, in which it is sheltered from reacting with cellular oxidants and electrophiles. (c) The active site loop of chain B shown adopting both the FF path (solid white) and the LU_{SH} path (solid yellow) with similar levels of $2F_O$-F_C electron density (countered at 1.0 ρ_{rms}). The LU_{SH} conformation is similar to that of LU_{S-S} (transparent forest green; PDB code 1yep), but the C_P thiol adopts a different position.

a partially occupied sulfhydryl from DTT (present at ~0.1 M) that binds at this site when the C-terminus is not folded. Both mass spectrometry on these crystals (Figure S2 of the Supporting Information) and reasonably clear electron density for Ala165 in chain A confirm that the crystals are of the C165A mutant. Using the reference restraint option of Phenix[41], the WT_{DTT} structure was utilized to restrain the geometries of the weakly occupied C-terminal regions. Riding hydrogens were added to the model, and one TLS group per chain was implemented to reach final R/R_{free} values of 19.8%/23.9% (Table 1). The coordinates and structure factors for the WT_{DTT} and $C165A_{DTT}$ structures have been deposited in the Protein Data Bank as PDB codes 4ma9 and 4mab.

Mass Spectrometry Analysis. Crystal samples were prepared from crystals harvested into a 10 μL drop of degassed deionized water, manually crushed, and kept from further chemical reactions by flash-freezing them in liquid nitrogen prior to analysis. Proteins were detected from 800 to 2000 m/z using a LTQ-FT Ultra mass spectrometer (Thermo, San Jose, CA, US) in LTQ mode, with a Finnigan Ion Max API source set up for electrospray ionization in positive ion mode. All collections used the following conditions: spray voltage 5 kV, capillary temperature 200 °C, capillary voltage 40 V, and tube lens voltage 240 V. Proteins from samples described above were adsorbed onto a C4 Ziptip, washed with water, and eluted inline to the mass spectrometer with solvent as previously described.[42,43] The solvent of 50% acetonitrile, 50% water, and 0.1% formic acid was delivered at 20 μL/min. Maximum entropy deconvolution and integration of the mass spectrum was performed to generate zero charge parent masses from the mass spectra using the program MOP (Multiple Overlaying Pictures, Spectrum Square Associates, Inc.) and Matlab.[42] Spectra of crystals were noisy but clearly showed that WT_{DTT} was predominantly monomeric (indicating reduction of the intermolecular disulfide; Figure S1 of the Supporting Information) and $C165A_{DTT}$ was mostly in the thiol/thiolate state, though there were minor peaks near the expected positions of C_P-SOH, C_P-SO_2^-, and C_P-SO_3^- (Figure S2 of the Supporting Information). The time course assay for C165A was performed on reduced protein at 43.5 μM in 100-fold diluted PBS buffer,[44] pH 7.0, with the addition of peroxide to make the final concentration 1 mM. Samples were taken at 0, 1, 2, 3, 5, 10, and 20 min and analyzed as specified above.

RESULTS AND DISCUSSION

Overall Structure. Recognizing that the existing *St*AhpC wild-type LU_{S-S} structure[22] had few crystal contacts involving residues that change positions in the FF↔LU transition (Figure 1b), we conceived of generating the FF conformation by soaking the LU_{S-S} crystals in DTT. Fresh crystals of the disulfide form of wild-type *St*AhpC[22] survived the DTT soak with diffraction power and unit cell virtually unchanged, allowing the structure to be determined at 1.82 Å resolution using recently proposed[36] more generous resolution cutoff criteria (Table 1). We identified bound potassium and chloride ions (Figure 2), which may relate to how ionic strength can increase decamerization, FF stability, and catalytic activity,[29] as has been reported for another AhpC.[45] In this crystal form a half-decamer of five chains (labeled A−E) are in the asymmetric unit, with the AB, CD, and EE_{sym} (symmetry mate of E) pairs being the functional homodimer units (Figure 1b).[22,29] For the wild-type DTT-treated structure (WT_{DTT}), disulfide reduction did occur, as the active site loop (residues 40−50) for chains A, C, D, E, and the C-termini of their partner chains (B, D, C, and E_{sym}, respectively) adopt the FF conformation, and the C_P and C_R thiolates/thiols are visible in their expected positions ~14 Å apart (Figure 3a,b). Mass spectrometry of dissolved WT_{DTT} crystals confirmed the presence of the reduced monomeric form (Figure S1 of the Supporting Information). Interestingly, the active site loop of chain B exhibits a ~50:50 mix of the FF/LU chain paths (Figure 3c), and its partner in the dimer, chain A, has its C-

dx.doi.org/10.1021/bi4011573 | *Biochemistry* 2013, 52, 8708−8721

Table 2. Conformations and Their Occupancies As Seen in Representative Active Sites of *St*AhpC Structures[a]

Crystal : active sites	FF	$LU_{C\text{-}term}$	LU_{SH}	$LU_{S\text{-}S}$
	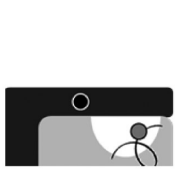			
WT_{DTT} : AB′, CD′, DC′, EE′	100	0	0	0
WT_{DTT} : BA′	0	50	50	0
$C165A_{DTT}$: AB′, CD′, DC′, EE′	60	20	20	0
$C165A_{DTT}$: BA′	0	50	50	0
C46S : all 20	100	0	0	0
$WT_{S\text{-}S}$: all 5	0	0	0	100

[a]The conformation names used are all described in the text, and the cartoon images provide a simple visual of the essential features of the conformation with the C_P shown as a gray circle and C_R as a black circle. The four crystal forms listed are also described in the text.

terminus LU (only modeled through residue 163) even though no C_P—C_R disulfide is present (Figure 1a). This C-terminal LU conformation can be explained in that a crystal packing interaction blocks the position it would fill in the FF conformation (Figure 1b).

Thus, in this crystal, three new conformations containing reduced C_P and C_R residues are observed (Table 2). One, as targeted, is the FF conformation adopted by the wild-type enzyme that is seen four times in the asymmetric unit, which we refer to as FF_{WT} (Figure 3a,b). The others are both ∼50% occupied and pair an LU C-terminus with either an LU active site loop without a disulfide (LU_{SH}) or with an FF active site loop ($LU_{C\text{-}term}$) (Figure 3c). For clarity, since each complete active site combines residues from two chains, we will use here a nomenclature that first defines the chain contributing C_P and then the chain contributing C_R, and using a prime (′) to denote residues from the chain contributing C_R. Thus, the four ∼100% FF_{WT} active sites are the AB′, CD′, DC′, EE'_{sym} active sites, and the 50:50 mix of the LU_{SH} and $LU_{C\text{-}term}$ conformations occurs in the BA′ active site. An advantage of this crystal form is that it provides a controlled environment in which *St*AhpC structures are each seen in two basic contexts—one with unconstrained C-termini and active site loop regions (active sites AB′, CD′, DC′, and EE'_{sym}) and one with a C-terminus constrained to be unfolded and unconstrained active site loop (active site BA′). A summary of the conformations seen in *St*AhpC structures compared in this paper is given in Table 2.

Linkage of the Active Site Loop and C-Terminal Conformations. *Asymmetry of Interactions Linking the C-Terminal and Active Site Loop Regions.* As noted above, for the BA′ active site, the A-chain C-terminal region is blocked from adopting the FF conformation by a crystal contact. Our observance of the $LU_{C\text{-}term}$ conformation in this active site proves that the active site loop can be FF even when the C-terminal region is LU. In addition, because the BA′ active site loop was ∼50% LU (as opposed to dominantly FF as for the other active sites), we infer a thermodynamic linkage in which the absence of a folded C-terminal region destabilizes the FF active site loop.

Comparing the FF_{WT} and LU_{SH} structures in the region of the active site (Figure 4a) shows that unfolding of the C-terminus could destabilize the active site loop in three ways. The first way is the loss of hydrophobic packing interactions between Leu176′, Leu182′, and Ile186′ side chains and the first turn of helix α2. The second way is a less direct effect, mediated by residues 137−142 which in the FF conformation make a short β-sheet with C-terminal residues 163′−166′ (Figure 4a). When 163′−166′ move away in the LU transition, the 137−142 segment shifts ∼1.5 Å, pulling with it Glu49 which is H-bonded with 142-NH (Figure 5). This shifting of the Glu49 and Glu138 carboxylates contribute to a disordering of Arg119 and the weakening of its interactions with the FF C_P side chain (Figure 5). The third way, a contribution not relevant for the crystalline decamer but expected to occur in solution, is that the loss of the packing from the side chains of Leu180′ and Val183′ with a hydrophobic niche (residues 15−20) at the decamer-building interface (Figure 4a) would destabilize the decamer and therefore, as has been noted before,[22] destabilize the active site loop.

In these ways, the unfolding of the C-terminus destabilizes but does not force the unfolding of the FF active site loop. In contrast, the unfolding of the active site loop will not just destabilize the C-terminal segment but will actually *force* that segment to unfold (Figure 4b). This asymmetric linkage occurs because the LU positions of the active site loop backbone physically collide with the FF positions of Leu176′, Leu182′, and Ile186′.

Active Site Loop and C-Terminal Region B-Factor Patterns Provide Additional Evidence of Linkage. For the AB′, CD′, DC′, and EE'_{sym} active sites in this crystal form, both LU_{S-S} (as grown) and FF (after reduction by DTT) conformations can be adopted, proving that the mobility of these active sites are not hindered by the crystal packing. Therefore, additional evidence of a physical linkage between the active site loop and C-terminal conformations can be gleaned from their *B*-factors, which show that a correlation exists between their dynamic properties, with more ordered active site loops (lower *B*-factors) paired with more ordered C-termini (Figure 6 inset).

dx.doi.org/10.1021/bi4011573 | *Biochemistry* 2013, 52, 8708−8721

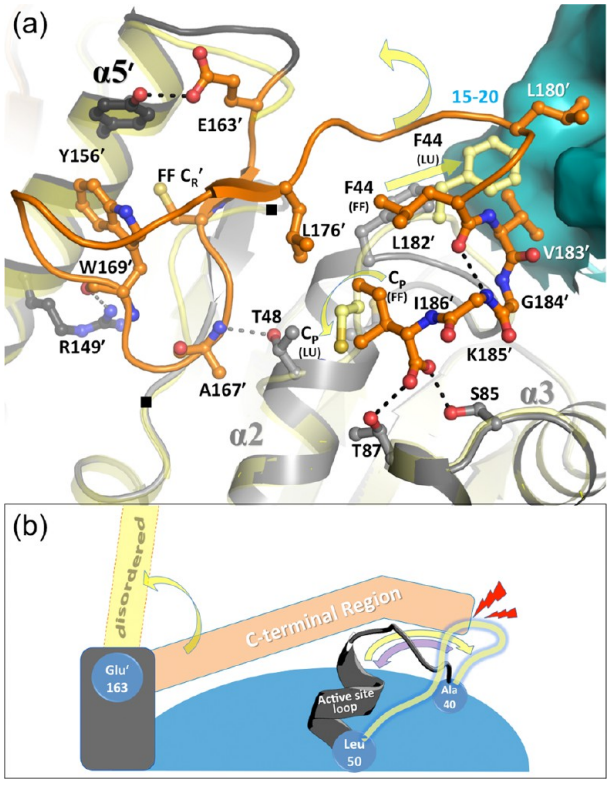

Figure 4. Packing interactions and coordination of unfolding of the FF C-terminal and active site loop regions. (a) The FF active site is shown (active site loop in gray; C-terminal region in dark orange; and the neighboring surface across the decamer-building interface in cyan) along with select interacting residues (labeled and shown as sticks) and stabilizing hydrogen bonds (dashed lines). Positions of residues 137 and 141 are also noted (■). To provide context, the LU_{SH} conformation (transparent yellow) is shown, and yellow arrows indicate movements of the C_P residue and Phe44. The C-terminal region has minimal regular secondary structure (residues Val164′–Cys165′ form a short β-strand, and Leu180′–Gly184′ is a short 3_{10}-helix), and it interacts with helix α5′ of the same chain (two H-bonds shown), across the decamer-building interface, and with the FF active site loop. The C-terminal residue Ile186′ side chain packs with Pro47, and C-terminal α-carboxylate H-bonds with the side chains of Ser85 and Thr87. (b) Cartoon scheme emphasizing that C-terminal region unfolding destabilizes but does not disrupt the active site loop, whereas active site loop unfolding does disrupt the folding of the C-terminal region. As in panel a, FF conformations of the two regions are shown in gray and orange; yellow arrows indicate transitions to LU, and LU positions are depicted in transparent yellow. Shown also are approximate hinge points at Ala40, Leu50, and Glu163′ (blue cogs) and the collision of the LU active site loop with the FF C-terminal region (red lightning). The purple arrow emphasizes that the active site loop is not blocked from folding. The decamer-building interactions are not shown in this scheme.

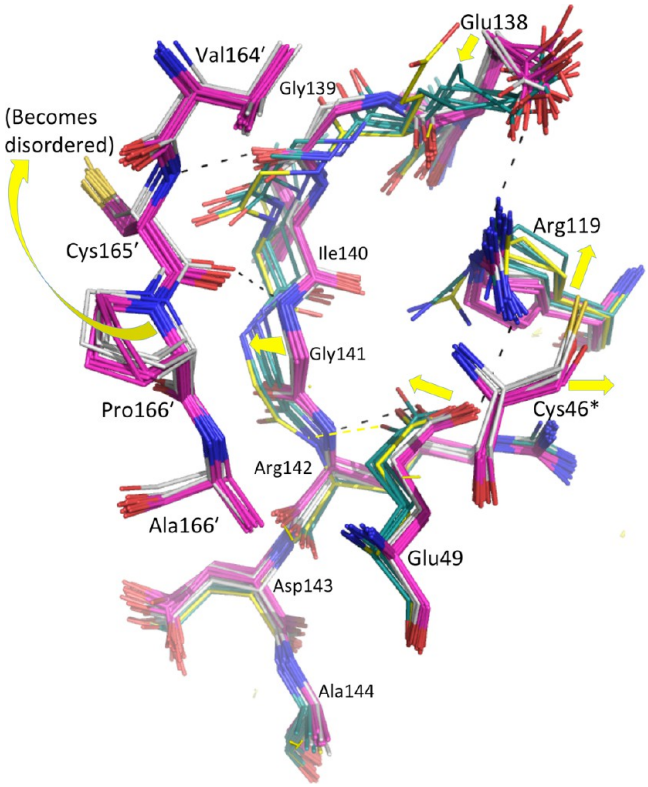

Figure 5. Role of the 137–142 segment in the FF↔LU transition. Shown are 24 FF dimers (C46S, pink; wild-type, white) and 6 LU dimers (LU_{S-S}, forest green; LU_{SH}, yellow), with yellow arrows highlighting FF→LU shifts. For clarity, only the FF position of C_P (C46 or S46, denoted with an asterisk) is shown. Select H-bonds shown link residues 139–141 in a β-sheet with the FF C-terminal region and, via the Glu138 and Glu49 side chains, to the catalytic Arg119.

The detailed *B*-factor patterns of the chains, controlled for the crystal environment, further illustrates this linkage. Interestingly, all five regions associated with the FF↔LU transition are the high *B*-factor peaks, and of these, three regions—the active site loop, the C-terminus, and residues 85–87 which H-bond to the Ile186′ α-carboxylate—become even more disordered in the transition from FF_{WT} to LU_{S-S} (black vs green curves in Figure 6). That all five segments are rather mobile in both FF_{WT} and LU_{S-S} leads us to conclude that they are easily adaptable rather than being highly stabilized in either conformation, and this helps keep the energy barrier to the conformation change low.

Changes Associated with the C_P→Ser Mutation. *Positional Differences in the FF Active Site.* In addition to *St*AhpC, many structures of FF Prx enzymes have only been solved as C_P→Ser mutants,[46−53] assuming that a Ser in the reactive C_P position faithfully mimics the active site. Given that an active site Cys→Ser mutation can alter the thermodynamics of a folded protein sufficiently to cause substantial rearrangement of the active site,[54,55] we looked for differences caused by the C46S mutation by comparing the 4 FF_{WT} active sites with the 20 independent FF active sites seen in crystals of the C46S mutant (FF_{C46S})[10] (Figure 7a). Although the FF_{WT} and FF_{C46S} structures are very similar (root-mean-square deviation (rmsd) ~0.35 Å for 186 C_α-atoms), the sets of FF_{WT} and FF_{C46S} structures cluster distinctly (Figure 7a), revealing systematic active site differences. For clarity in this comparison, we refer to the C46S mutant structure as being "shifted" relative to the wild type.

Despite conservation of the C_P backbone position, Ser46-Oγ is shifted consistently by ~1 Å compared to Cys46-Sγ, is further from Ala40-NH, Thr43-Oγ, and Arg119-NH2, and is closer to Arg119-NH1 (Figure 7a). Also, the side chains of Arg119 and Pro39 shift slightly, and Thr43 sits deeper in the active site pocket. Independent evidence that shows which of these shifts are due to the Cys→Ser mutation can be gleaned from the prototypical Prx substrate-bound structures of *Aeropyrum pernix*

dx.doi.org/10.1021/bi4011573 | *Biochemistry* 2013, 52, 8708–8721

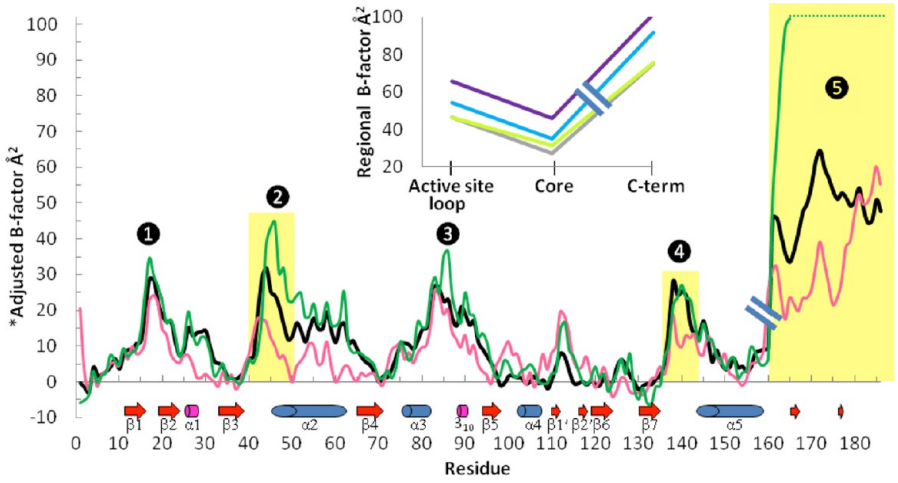

Figure 6. Mobility patterns in wild-type *St*AhpC and C_P→Ser structures. A hybrid plot of average main chain *B*-factors by residue is shown, with each color trace representing the *B*-factors for residues 1−160 of one chain and residues 161−186 of its dimer partner chain. Shown are the wild-type FF AB′ dimer (black), the LU_{S-S} AB′ dimer (PDB code 1yep; forest green), and a dimer from FF C46S with a solvent exposed active site (PDB code 1n8j KL′ dimer; pink). To normalize comparisons, the *B*-factors were adjusted by subtracting a trace-specific "core" *B*-value (defined as the 10th percentile *B*-factor of atoms in the chain contributing residues 1−160). Indicated below the plot are the positions of secondary structures (labeled). The peaks labeled 1 to 5 are the segments involved in the FF↔LU transition, with regions that move highlighted in gold. In C46S, the less-ordered N-terminus may be due to the lack of a chloride ion in this crystal form, and the low *B*-factors near residue 30 are due to a crystal packing interaction. Differences in the 100−130 region may be attributed to the unidentified ligand at the decamer-building interface (see Supporting Information, Figure S3). Inset: Plotted are the average main chain *B*-factor for residues 40−50 (active site loop) and for residues 161′−186′ (C-term), along with the 10th percentile *B*-value of the active site loop containing chain (core) for each of the four FF_{WT} active sites: AB′ (gray), CD′ (lime green), DC′ (blue), and EE'_{sym} (purple). The variation in absolute mobility among the four FF_{WT} active sites relates to the crystal packing interactions, with, for example, the EE'_{sym} active site being the most disordered, because it has no crystal contacts (see also Figure 1b).

thiol peroxidase (*Ap*Tpx, a Prx6 family member despite the Tpx name;[1] PDB code 3a2v)[56] (Figure 3a) and the diol inhibitor-bound *Homo sapiens* PrxV (*Hs*PrxV; PDB code 3mng),[24] which fortuitously have high resolution structures available for both the wild type and C_P→Ser forms.[1] In both cases, similar shifts are seen for the Ser, Arg, and Thr side chains, and these structures additionally show that bound ligands sit more deeply in the active site of the C_P→Ser mutants (Figure 7b,c).

In rationalizing these common shifts, we assume, for a few reasons, that the C_P residue in the wild-type structures is present as the catalytically relevant thiolate: first, the *St*AhpC crystals are grown at pH ∼6.5, above the experimentally measured C_P pK_a of 5.9 ± 0.1;[23] second, the peroxide-bound *Ap*Tpx crystals (PDB code: 3a2v) were at pH 6.5 and were catalytically active;[24] third, all the *Hs*PrxV structures, ranging from pH = 5.6 to 8.0, adopt a similar active site geometry;[24] and fourth, the interactions between Sγ and its active site surroundings are compatible with the thiolate interpretation (Figure 7). We expect that a hydroxyl would not be able to perfectly mimic a thiolate, as the thiolate is larger (van der Waals radius ∼0.7 Å greater), cannot donate a hydrogen bond, and with its more diffuse electron clouds is "softer," making for rather different H-bonding properties.[57,58] We attribute the Ser and Arg shifts to making the Arg119-NH1···Oγ H-bond shorter and better aligned in the mutant, and the Thr shift as filling in the space opened by the Sγ to Oγ change while improving the linearity of its H-bond with the backbone carbonyl.[59] The ∼0.5 Å deeper penetration of ligands into the active sites of C_P→Ser mutants (Figure 7b,c) would be due to both the smaller van der Waals radius of oxygen and the formation of a Ser-OγH···ligand H-bond. Given such structural differences it should not be surprising that the C46S mutation may also have thermodynamic consequences.

B-Factors and Crystallizability Indicate Mutation-Induced Alterations to Mobility. Beyond the changes in atom positions, we also observed striking differences between the *B*-factors of FF_{WT} and a FF_{C46S} active site that is not constrained by crystal contacts (Figure 6). Relative to their respective cores, FF_{C46S} has *B*-factors about half as high as the FF_{WT} in all three regions of the structure that change positions in the FF↔LU transition (yellow highlights). This greater order of C46S provides evidence that in some way the C_P-Ser mutation has a stabilizing effect on the FF active site, and we propose that this apparent stabilizing effect is at least in part because the Ser−Arg hydrogen bond (Figure 7a) is stronger than those formed by the sulfur atom.[58] The *Ap*Tpx and *Hs*PrxV C_P→Ser structures do not share this difference in *B*-factor patterns, but this may be due to a stabilizing effect of the bound inhibitors and/or crystal packing interactions.

Additional evidence for a difference in the dynamic properties of C46S and wild-type *St*AhpC is that we were not able to crystallize the reduced wild-type enzyme in the C46S mutant *P*1 spacegroup,[10] despite the near identity of their average structures. The explanation we propose is that even though the FF conformation is dominant for the reduced wild-type enzyme, LU or partially LU conformations are present at a high enough level to prevent growth of the *P*1 crystals, which have some packing interactions that are not compatible with the LU conformation. This is consistent with deuterium exchange analysis of reduced wild-type *St*AhpC that revealed the active site loop to be the least protected region.[60] These differences in *St*AhpC induced by the C_P→Ser mutation reinforce two things: first, one must be cautious when inferring the properties of the wild-type enzyme from studies of such variants, and second, that the wild-type active site has not evolved to be as highly stable as possible, as it would be counter-productive to catalysis (see also below).

dx.doi.org/10.1021/bi4011573 | *Biochemistry* 2013, 52, 8708−8721

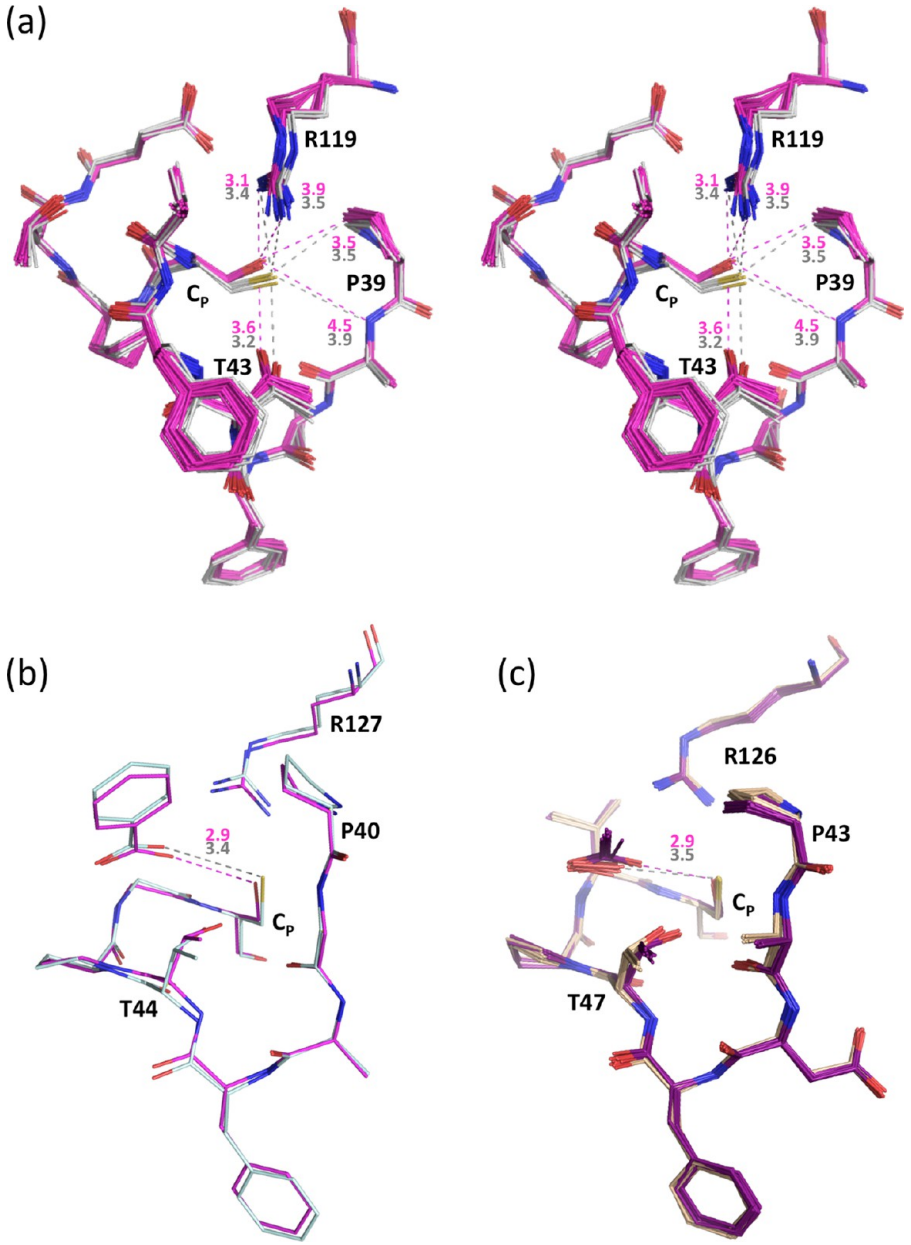

Figure 7. Active site changes due to C_P→Ser mutations. (a) Stereodiagram of 20 chains of C46S (pink) overlaid onto the 4 chains of wild-type *St*AhpC (solid white), with representative distances given in Å based on C46S chain K (pink) and wild-type chain A (gray). Estimation of coordinate uncertainty by SFCHECK[68] for both of these models is in the range of 0.2−0.3 Å. (b) Active site overlay of wild-type *Hs*PrxV (light blue, PDB code 1hd2) and its C_P→Ser mutant (pink, PDB code 1urm) with color-coded distances to the bound benzoate indicated, which were chosen for comparison on the basis of having resolution better than 2.0 Å, clear density for the ligands, and adoption of the same space group with similar unit cells. For 12 chains of wild-type *Hs*PrxV with benzoate, acetate, or DTT ligands (PDB codes 1hd2, 3mng, 1h4o, 1oc3, 2vl2, and 2vl3) the average Cys Sγ···ligand distance is 3.46 Å (c) Active site overlay of 10 chains from wild-type *Ap*Tpx (light pink, peroxide-bound; PDB code 3a2v) and 10 chains from its C_P→Ser mutant (purple, acetate bound; PDB code 3a2x) with the color-coded average distances indicated.

Structural Characterization of the *St*AhpC C_R→Ala Mutant. Recently a study of *Hs*PrxIV crystals that could accommodate both the FF and LU conformations showed that a resolving Cys→Ala mutant (*Hs*PrxIV-C245A) adopted the FF conformation when reduced, but was LU after a 5 min 1 mM peroxide treatment said to generate the C_P-SOH form.[27] Because of the apparent resistance of the C_P-SOH to further oxidation, the authors concluded that once the newly formed C_P-SOH transitions to LU, "it does not reform the FF conformation until the peroxidatic Cys is reduced."[27] However, we note that a Western blot of similar treatments in that study showed that an unquantified portion of the sample was hyperoxidized to C_P-$SO_{2/3}$, and the identification of the C_P-SOH state was only based on interpreting an electron density map that for some chains showed alternate conformations for the C_P side chain. To address this important point further, we sought to use our *St*AhpC crystal form to crystallographically define thermodynamic impacts on the FF↔LU equilibrium of both a C_R→Ala mutation and C_P-SOH formation.

β-Mercaptoethanol (BME) as a Crystallization Aid. We generated the equivalent *St*AhpC C_R→Ala mutant (C165A), which as expected was active in the presence of a suitable

dx.doi.org/10.1021/bi4011573 | *Biochemistry* 2013, 52, 8708−8721

reductant. As purified, the C165A variant did not readily crystallize, but crystal growth was strongly promoted by treatment with 100 mM hydrogen peroxide, and the resulting structure showed the protein in the LU conformation in what, based on the electron density, we originally modeled as the C_P-SOH form (data not shown). However, mass spectrometric analyses of the crystals (Figure S2 of the Supporting Information) showed them to be a roughly 60:40 mix of a BME adduct (presumably a mixed disulfide with C_P) and C_P-SO_3 despite the lack of clear density for these modifications. Using this insight we created a C165A BME–adduct crystal by exposure to only μM levels of peroxide in the presence of added BME. We suggest on the basis of this experience that, especially for C_R mutants or 1-Cys Prxs, trapping an otherwise dynamic Prx enzyme (e.g., ref 26) in an LU mixed-disulfide state (for instance, with BME) may enhance conformational homogeneity and serve as a generally useful crystallization aid.

The Structure of Reduced C165A. The BME–adduct crystal was soaked with DTT to yield a 1.9 Å resolution structure of reduced *St*AhpC C165A (Table 1; Figure S2a of the Supporting Information). In this $C165A_{DTT}$ structure, the BA′ active site (in which the C-terminal region cannot fold) is like WT_{DTT} adopting a 50:50 mix of the LU_{SH} and $LU_{C\text{-}term}$ conformations. However, for the other four active sites, the active site loops are visibly in the FF conformation with an unmodified C_P side chain (Figure S2b of the Supporting Information), but the C-termini have very weak electron density and were modeled at ~60% FF (Table 2). As little, if any, C_P oxidation is present, the ~40% unfolding of the C-termini must reflect a destabilization caused by the C165A mutation itself. A mutation of a Cys→Ala in a buried, nonpolar environment is expected to be destabilizing.[61]

Time Course of C165A Oxidation Implies a Dynamic C_P-SOH Form. To seek conditions for generating pure C165A C_P-SOH for crystallographic study, we used mass spectrometry to characterize its peroxide-driven C_P oxidation. The time course reveals that S-BME and SOH forms appear early, and that as the BME is used up, the SOH peak smoothly decreases while the SO_2^- peak increases (Figure 8). This conversion implies that the *St*AhpC C_P-SOH form is not locked into the LU conformation but dynamically adopts the FF conformation from which it reacts with a second peroxide to form C_P-SO_2^-. Given this behavior, we were not able to create a pure C165A C_P-SOH species for structural analysis.

The facile hyperoxidation of the *St*AhpC C165A variant is an expected result and makes all the more surprising the report that *Hs*PrxIV-C245A[27] resists hyperoxidation sufficiently to be crystallized as a stable C_P-SOH form. Although the two proteins may behave this differently, another possibility is that despite the electron density map evidence, the peroxide-treated *Hs*PrxIV-C245A structure was not C_P-SOH, but a mixture of C_P-SOH, C_P-SO_2^-, C_P-SO_3^- and/or mixed disulfide forms. Our experience noted above with the structure of C165A treated with 100 mM peroxide (in which we had satisfactorily modeled C_P-SOH into the electron density maps of protein that was a mixture C_P-SO_3^- and a BME adduct) shows that electron density alone in an exposed region of a structure may be insufficient to differentiate between C_P-SOH and higher oxidation states. While we agree that C_P-SOH formation may indeed promote unfolding of the active site, we suggest that mass spectrometric characterization of the peroxide-treated *Hs*PrxIV-C245A is needed before firm conclusions are drawn.

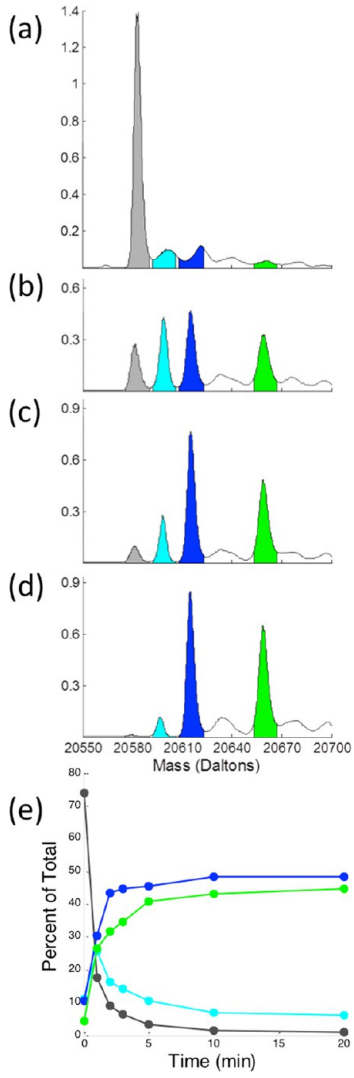

Figure 8. Modifications of C165A *St*AhpC by 1 mM hydrogen peroxide. (a–d) Mass spectra of purified C165A *St*AhpC starting material before and after treatment with 1 mM peroxide for 1, 3, and 20 min, respectively (see Experimental Procedures). The theoretical weight of C165A is 20584.32 Da ($C_{928}H_{1427}N_{241}O_{283}S_3$); with the modifications, it is 20600.32 Da (+1 oxygen), 20616.32 Da (+2 oxygens), and 20660.44 Da (BME adduct, + C_2H_4OS). Experimental peaks have values of 20584 Da (gray), 20599 Da (cyan), 20615 Da (blue), and 20659 Da (green). Inferred identities of the observed species assume that additions are associated with the C_P residue. The *y* axes are normalized so that the summed areas of the four colored peaks is a constant. (e) Integrated normalized populations of four prominent species as a function of time. We suspect that the time = 0 populations attributed to SOH (cyan) and SO_2^- (blue) are overestimates, because the peak centers are not at the expected mass, and they may be satellite peaks caused by some noncovalent ligand binding to the fully reduced protein. Fortunately, these areas are small, and their inclusion does not substantially impact the conclusions.

A Conceptual Model for Understanding the Impact of Prx Modifications on Activity. The changes in conformation and equilibrium populations that we have observed highlight the extent to which even slight modifications in or near the Prx active site can alter the enzyme's properties. Although the variety of effects appears complex, a simple thermodynamic model for how the various modifications stabilize or destabilize

dx.doi.org/10.1021/bi4011573 | *Biochemistry* 2013, 52, 8708–8721

the FF active site can account for the range of structural changes seen and help in understanding the implications those changes have for function (Figure 9). The six curves illustrate

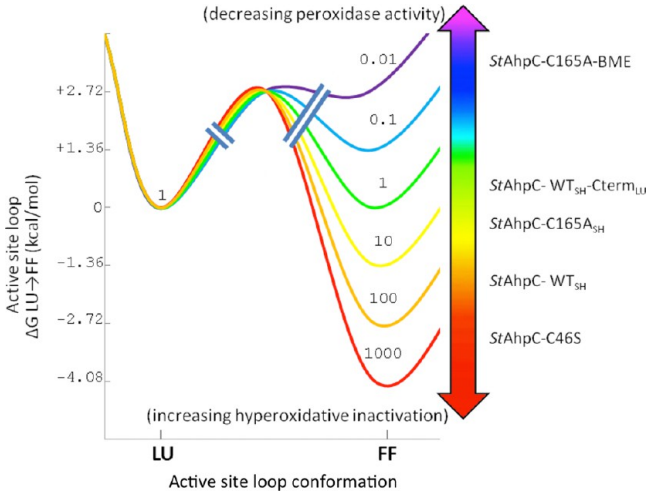

Figure 9. A thermodynamic framework for understanding the impact alteration of the active site loop FF↔LU equilibrium has on Prx function. Plotted is an illustrative series of six possible free energy changes associated with the LU to FF transition, with each 1.36 kcal/mol increment in its relative stability corresponding to a 10-fold change in the FF/LU equilibrium ratio at 298 K. The transition-state barrier is not to scale, but for simplicity, we have drawn it to be relatively low, consistent with the rapid dynamics seen for some Prxs.[26] On the basis of the relative strength of density observed for the FF and LU conformations in various crystal forms and active sites, we have roughly assigned the structures discussed here to the different curves. Along this series, the *St*AhpC forms discussed in the text are shown at the point at which we approximate their FF↔LU equilibria. As illustrated by the arrows, modifications that destabilize the FF active site will lower the initial rate of reaction with peroxides while protecting against hyperoxidation, whereas modifications that stabilize the FF will slow disulfide formation and increase the enzyme's susceptibility to hyperoxidation. These effects could, in theory, also be induced by inhibitors that stabilized either the LU or FF conformation.

that changes in interaction energies of just a few kcal/mol can shift the FF↔LU equilibrium from 1000:1 to 1:100. The crystal structures analyzed here show a hierarchy of FF↔LU equilibria (Table 2) that allows us to assign various *St*AhpC forms to the different curves (Figure 9). Beginning with the most ordered FF active site, the *St*AhpC C46S mutant seems to be in the range of the orange to red curves (99.9−99% FF). The four FF_{WT} active sites that are visibly FF (but less so than C46S) might be represented by the orange to yellow curves (99−90% FF), while the equivalent active sites in the $C165A_{DTT}$ structure—with the C-terminal region destabilized relative to the wild type—would be between the yellow and green curves (90−50% FF). The BA′ active site of the WT_{DTT} structure with its ∼50:50 mix of $LU_{SH}/LU_{C\text{-}term}$ conformations is described by the green curve. Lastly, the BME adduct that strongly destabilizes the FF active site loop would be represented by the violet curve or above (≥99% LU). Two key insights from these analyses are that (1) for wild-type *St*AhpC the FF:LU free energy difference is not large, so even minor changes can substantially impact the enzyme's properties, and (2) given this sensitive positioning, the FF-stabilizing C_P→Ser mutation and the FF-destabilizing C_R→Ala mutation may each sufficiently perturb the FF↔LU equilibrium such that the measured properties of those mutants will not reliably report on the properties of the wild-type enzyme.

Though each Prx enzyme will have distinct properties, these concrete examples of the linkage between sequence, structure, and thermodynamics can be applied to understand the impact of how sequence variations and physiological Prx post-translational modifications such as Thr/Ser phosphorylation and Lys acetylation, many of which occur in or affect the FF C-terminal region,[10,11,13,16−19] may regulate the enzyme's activity and/or its sensitivity to hyperoxidation by altering the FF↔LU equilibrium. Indeed, mutations disrupting the C-terminal region of certain Prxs allowed the enzymes to retain activity and become much less sensitive to inactivating hyperoxidation.[62,63] Similarly, in vivo proteolytic C-terminal truncation[20] or the acetylation of *Hs*Prx1 at Lys197[18] have both been reported to lower the enzyme's susceptibility to hyperoxidation, as is expected if they destabilize the C-terminal packing.

Targeting the Prokaryotic Prx C-Terminal Region for Drug Design. Although it is most common to target the active sites of proteins for drug therapy, inhibitors that trap enzymes in conformations in which catalysis cannot occur offer an alternative strategy. A recent example is a small-molecule inhibitor that holds a tumor-associated mutant of isocitrate dehydrogenase 1 in an open and unreactive conformation.[64] As Prxs contain a universally conserved active site, yet exhibit highly divergent C-terminal regions, especially between human and prokaryotic homologues,[1] this latter strategy could be very useful for developing inhibitors selective for pathogen Prxs.[10,44] In particular, our observations here lead us to suggest three novel strategies for developing antibiotics that could diminish prokaryotic redox defenses through blocking Prx activity. First, molecules that disrupt the C-terminal packing (indicated by the upward arrow in Figure 9) would decrease the amount of FF enzyme present and thus inhibit the enzyme's peroxidase activity. Second, and somewhat counterintuitive, even more effective could be molecules capable of highly *stabilizing* the FF C-terminus of prokaryotic Prxs (indicated by the downward arrow in Figure 9). These would strongly shift the equilibrium toward FF to promote (potentially to 100%) the hyperoxidation of C_P so that inactive C_P-$SO_{2/3}^-$ states would accumulate. Third, in a special case that combines these effects, an inhibitor that both destabilized the FF active site and also blocked resolution of the C_P-SOH state (similarly to the behavior of the *St*AhpC-C165A mutant) would both decrease peroxidase activity and promote formation of the hyperoxidized forms. Because few prokaryotes possess a sulfiredoxin-type enzyme capable of reversing hyperoxidation of the peroxidatic Cys,[11] the latter two approaches could be extremely effective, as the hyperoxidation to C_P-$SO_{2/3}^-$ would cause permanent inactivation.[65]

■ ASSOCIATED CONTENT

Supporting Information

Mass spectrometric data of wild-type *St*AhpC crystals showing the shift from dimer to monomer when soaked with DTT (Figure S1); mass spectrometric and crystallographic characterization of the C165A mutant crystals (Figure S2); uninterpreted ligand density at the decamer-building interfaces (Figure S3). This material is available free of charge via the Internet at http://pubs.acs.org.

AUTHOR INFORMATION

Corresponding Author

*E-mail: karplusp@science.oregonstate.edu. Tel.: 541-737-3200. Fax: 541-737-0481.

Funding

This study was supported in part by National Institutes of Health Grant RO1 GM050389 to L.B.P. and P.A.K.

Notes

The authors declare no competing financial interest.

ACKNOWLEDGMENTS

The mass spectrometric analyses were enabled by the Oregon State University Environmental Health Science Center supported by NIEHS Grant #P30 ES000210, and crystallographic data collection was done at the Advanced Light Source (ALS), supported by the Director, Office of Science, Office of Basic Energy Sciences, of the U.S. Department of Energy under Contract No. DE-AC02-05CH11231.

ABBREVIATIONS:

Prx, peroxiredoxin; *St*AhpC, *Salmonella typhimurium* alkyl hydroperoxide reductase component C; FF, fully folded; LU, locally unfolded; C_P, peroxidatic Cys; C_R, resolving Cys; LU_{S-S}, locally unfolded disulfide form; LU_{SH}, locally unfolded thiol form; $LU_{C\text{-}term}$, C-terminally unfolded form; WT_{DTT}, DTT-treated wild-type structure; $C165A_{DTT}$, DTT-treated C165A structure; FF_{WT}, fully folded wild type; FF_{C46S}, fully folded C46S mutant; *Hs*PrxIV, *Homo sapiens* PrxIV; *Hs*PrxI, *Homo sapiens* PrxI; *Hs*PrxV, *Homo sapiens* PrxV; *Ap*Tpx, *Aeropyrum pernix* thiol peroxidase; PDB, Protein Data Bank; DTT, 1,4-dithiothreitol; BME, β-mercaptoethanol; MES, 2-(*N*-morpholino)ethanesulfonic acid; PBS, phosphate buffered saline; ALS, Advanced Light Source; NCS, noncrystallographic symmetry; TLS, translation-libration-screw; AML, artificial mother liquor; ρ_{rms}root mean square of electron density

REFERENCES

(1) Hall, A., Nelson, K., Poole, L. B., and Karplus, P. A. (2011) Structure-Based Insights into the Catalytic Power and Conformational Dexterity of Peroxiredoxins. *Antioxid. Redox Signaling 15*, 795−815.

(2) Winterbourn, C. C. (2008) Reconciling the Chemistry and Biology of Reactive Oxygen Species. *Nat. Chem. Biol. 4*, 278−286.

(3) Cox, A. G., Winterbourn, C. C., and Hampton, M. B. (2010) Mitochondrial Peroxiredoxin Involvement in Antioxidant Defense and Redox Signaling. *Biochem. J. 425*, 313−325.

(4) Chen, L., Xie, Q., and Nathan, C. (1998) Alkyl Hydroperoxide Reductase Subunit C (AhpC) Protects Bacterial and Human Cells against Reactive Nitrogen Intermediates. *Mol. Cell 1*, 795−805.

(5) Fang, F. C. (1997) Perspectives Series: Host/Pathogen Interactions. Mechanisms of Nitric Oxide-Related Antimicrobial Activity. *J. Clin. Invest. 99*, 2818−2825.

(6) Seaver, L. C., and Imlay, J. A. (2001) Alkyl Hydroperoxide Reductase Is the Primary Scavenger of Endogenous Hydrogen Peroxide in *Escherichia coli*. *J. Bacteriol. 183*, 7173−7181.

(7) Cosgrove, K., et al. (2007) Catalase (KatA) and Alkyl Hydroperoxide Reductase (AhpC) Have Compensatory Roles in Peroxide Stress Resistance and Are Required for Survival, Persistence, and Nasal Colonization in *Staphylococcus aureus*. *J. Bacteriol. 189*, 1025−1035.

(8) Baker, L. M. S., Raudonikiene, A., Hoffman, P. S., and Poole, L. B. (2001) Essential Thioredoxin-Dependent Peroxiredoxin System from *Helicobacter pylori*: Genetic and Kinetic Characterization. *J. Bacteriol. 183*, 1961−1973.

(9) Mehta, N. S., Benoit, S. L., Mysore, J., and Maier, R. J. (1770) In Vitro and in Vivo Characterization of Alkyl Hydroperoxide Reductase Mutant Strains of *Helicobacter hepaticus*. *Biochim. Biophys. Acta 257*−*265*, 2007.

(10) Wood, Z. A., Poole, L. B., and Karplus, P. A. (2003) Peroxiredoxin Evolution and the Regulation of Hydrogen Peroxide Signaling. *Science 300*, 650−653.

(11) Rhee, S. G., Woo, H. A., Kil, I. S., and Bae, S. H. (2012) Peroxiredoxin Functions as a Peroxidase and a Regulator and Sensor of Local Peroxides. *J. Biol. Chem. 287*, 4403−4410.

(12) Giorgio, M., Trinei, M., Migliaccio, E., and Pelicci, P. G. (2007) Hydrogen Peroxide: A Metabolic by-Product or a Common Mediator of Ageing Signals? *Nat. Rev. Mol. Cell Biol. 8*, 722−728.

(13) Rhee, S. G., Yang, K. S., Kang, S. W., Woo, H. A., and Chang, T. S. (2005) Controlled Elimination of Intracellular H_2O_2: Regulation of Peroxiredoxin, Catalase, and Glutathione Peroxidase via Post-Translational Modification. *Antiox. Redox Signaling 7*, 619−626.

(14) Haque, A., Andersen, J. N., Salmeen, A., Barford, D., and Tonks, N. K. (2011) Conformation-Sensing Antibodies Stabilize the Oxidized Form of PTP1B and Inhibit Its Phosphatase Activity. *Cell 147*, 185−198.

(15) Kil, I. S., et al. (2012) Feedback Control of Adrenal Steroidogenesis via H_2O_2-Dependent, Reversible Inactivation of Peroxiredoxin III in Mitochondria. *Mol. Cell 46*, 584−594.

(16) Zykova, T. A., et al. (2010) T-LAK Cell-Originated Protein Kinase (TOPK) Phosphorylation of Prx1 at Ser-32 Prevents UVB-induced Apoptosis in RPMI7951 Melanoma Cells through the Regulation of Prx1 Peroxidase Activity. *J. Biol. Chem. 285*, 29138−29146.

(17) Chang, T.-S., Jeong, W., Choi, S. Y., Yu, S., Kang, S. W., and Rhee, S. G. (2002) Regulation of Peroxiredoxin I Activity by Cdc2-Mediated Phosphorylation. *J. Biol. Chem. 277*, 25370−25376.

(18) Parmigiani, R. B., Xu, W. S., Venta-Perez, G., Erdjument-Bromage, H., Yaneva, M., Tempst, P., and Marks, P. A. (2008) HDAC6 is a Specific Deacetylase of Peroxiredoxins and Is Involved in Redox Regulation. *Proc. Natl. Acad. Sci. U.S.A. 105*, 9633−9638.

(19) Park, J. W., Piszczek, G., Rhee, S. G., and Chock, P. B. (2011) Glutathionylation of Peroxiredoxin I Induces Decamer to Dimers Dissociation with Concomitant Loss of Chaperone Activity. *Biochemistry 50*, 3204−3210.

(20) Schröder, E., Willis, A. C., and Ponting, C. P. (1998) Porcine Natural-Killer-Enhancing Factor-B: Oligomerisation and Identification As a Calpain Substrate in Vitro. *Biochim. Biophys. Acta 1383*, 279−291.

(21) Nelson, K. J., Knutson, S. T., Soito, L., Klomsiri, C., Poole, L. B., and Fetrow, J. S. (2010) Analysis of the Peroxiredoxin Family: Using Active-Site Structure and Sequence Information for Global Classification and Residue Analysis. *Proteins: Struct., Funct., Bioinf. 79*, 947−964.

(22) Wood, Z. A., Poole, L. B., Hantgan, R. R., and Karplus, P. A. (2002) Dimers to Doughnuts: Redox-Sensitive Oligomerization of 2-Cysteine Peroxiredoxins. *Biochemistry 41*, 5493−5504.

(23) Nelson, K. J., Parsonage, D., Hall, A., Karplus, P. A., and Poole, L. B. (2008) Cysteine pKa Values for the Bacterial Peroxiredoxin AhpC. *Biochemistry 47*, 12860−12868.

(24) Hall, A., Parsonage, D., Poole, L. B., and Karplus, P. A. (2010) Structural Evidence that Peroxiredoxin Catalytic Power Is Based on Transition-State Stabilization. *J. Mol. Biol. 402*, 194−209.

(25) Perkins, A., Gretes, M. C., Nelson, K. J., Poole, L. B., and Karplus, P. A. (2012) Mapping the Active Site Helix-to-Strand Conversion of CxxxxC Peroxiredoxin Q Enzymes. *Biochemistry 51*, 7638−7650.

(26) Ådén, J., et al. (1814) Extraordinary μs—ms Backbone Dynamics in *Arabidopsis thaliana* Peroxiredoxin Q. *Biochim. Biophys. Acta, Proteins Proteomics 1880*−*1890*, 2011.

(27) Cao, Z., Tavender, T. J., Roszak, A. W., Cogdell, R. J., and Bulleid, N. J. (2011) Crystal Structure of Reduced and of Oxidized Peroxiredoxin IV Enzyme Reveals a Stable Oxidized Decamer and a Non-Disulfide-Bonded Intermediate in the Catalytic Cycle. *J. Biol. Chem. 286*, 42257−42266.

(28) Parsonage, D., Karplus, P. A., and Poole, L. B. (2008) Substrate Specificity and Redox Potential of AhpC, a Bacterial Peroxiredoxin. *Proc. Natl. Acad. Sci. U.S.A. 105*, 8209−8214.
(29) Parsonage, D., Youngblood, D. S., Sarma, G. N., Wood, Z. A., Karplus, P. A., and Poole, L. B. (2005) Analysis of the Link between Enzymatic Activity and Oligomeric State in AhpC, a Bacterial Peroxiredoxin. *Biochemistry 44*, 10583−10592.
(30) Baba, T., Ara, T., Haseqawa, M., Takai, Y., Okumura, Y., Baba, M., Datsenko, K. A., Tomita, M., Wanner, B. L., and Mori, H. (2006) Construction of *Escherichia coli* K-12 in-Frame, Single-Gene Knockout Mutants: the Keio Collection. *Mol. Syst. Biol. 2* (2006), 0008.
(31) Studier, F. W. (2005) Protein Production by Auto-Induction in High-Density Shaking Cultures. *Protein Expression Purif. 41*, 207−234.
(32) Poole, L. B. (1996) Flavin-Dependent Alkyl Hydroperoxide Reductase from *Salmonella typhimurium*. 2. Cystine Disulfides Involved in Catalysis of Peroxide Reduction. *Biochemistry 35*, 65−75.
(33) Sarma, G. N., Nickel, C., Rahlfs, R., Fischer, M., Becker, K., and Karplus, P. A. (2005) Crystal Structure of a Novel *Plasmodium falciparum* 1-Cys Peroxiredoxin. *J. Mol. Biol. 346*, 1021−1034.
(34) Mizohata, E., Sakai, H., Fusatomi, E., Terada, T., Murayama, K., Shirouzu, M., and Yokoyama, S. (2005) Crystal Structure of an Archaeal Peroxiredoxin from the Aerobic Hyperthermophilic Crenarchaeon *Aeropyrum pernix* K1. *J. Mol. Biol. 354*, 317−329.
(35) Battye, T. G. G., Kontogiannis, L., Johnson, O., Powell, H. R., and Leslie, A. G. W. (2011) iMOSFLM: a New Graphical Interface for Diffraction-Image Processing with MOSFLM. *Acta Crystallogr., Sect. D: Biol. Crystallogr. 67*, 271−281.
(36) Karplus, P. A., and Diederichs, K. (2012) Linking Crystallographic Model and Data Quality. *Science 336*, 1030−1033.
(37) Driggers, C. M., Cooley, R. B., Sankaran, B., Hirschberger, L. L., Stipanuk, M. H., and Karplus, P. A. (2013) Cysteine Dioxygenase Structures from pH 4 to 9: Consistent Cys-Persulfenate Formation at Intermediate pH and a Cys-Bound Enzyme at Higher pH. *J. Mol. Biol. 425*, 3121−3136.
(38) Evans, P. R., and Murshudov, G. N. (2013) How Good Are My Data and What Is the Resolution? *Acta Crystallogr., Sect. D: Biol. Crystallogr. 69*, 1204−1214.
(39) Smart, O. S., et al. (2012) Exploiting Structure Similarity in Refinement: Automated NCS and Target-Structure Restraints in BUSTER. *Acta Crystallogr., Sect. D: Biol. Crystallogr. 68*, 368−380.
(40) Emsley, P., and Cowtan, K. (2004) Coot: Model-Building Tools for Molecular Graphics. *Acta Crystallogr., Sect. D: Biol. Crystallogr. 60*, 2126−2132.
(41) Afonine, P. V., et al. (2012) Towards Automated Crystallographic Structure Refinement with Phenix.refine. *Acta Crystallogr., Sect. D: Biol. Crystallogr. 68*, 352−367.
(42) Rhoads, T. W., et al. (2011) Measuring Copper and Zinc Superoxide Dismutase from Spinal Cord Tissue Using Electrospray Mass Spectrometry. *Anal. Biochem. 415*, 52−58.
(43) Rhoads, T. W., Williams, J. R., Lopez, N. I., Morré, J. T., Bradford, C. S., and Beckman, J. S. (2013) Using Theoretical Protein Isotopic Distributions to Parse Small-Mass-Difference Post-Translational Modifications via Mass Spectrometry. *J. Am. Soc. Mass Spectrom. 24*, 115−124.
(44) Nelson, K. J., Parsonage, D., Karplus, P. A., and Poole, L. B. (2013) Evaluating Peroxiredoxin Sensitivity toward Inactivation by Peroxide Substrates. *Methods Enzymol. 527*, 21−40.
(45) Kitano, K., Niimura, Y., Nishiyama, Y., and Miki, K. (1999) Stimulation of Peroxidase Activity by Decamerization Related to Ionic Strength: AhpC Protein from *Amphibacillus xylanus*. *J. Biochem. 126*, 313−319.
(46) Matsumura, T., et al. (2008) Dimer-Oligomer Interconversion of Wild-type and Mutant Rat 2-Cys Peroxiredoxin Disulfide Formation at Dimer-Dimer Interfaces is not Essential for Decamerization. *J. Biol. Chem. 283*, 284−293.
(47) Smeets, A., Loumaye, E., Clippe, A., Rees, J. F., Knoops, B., and Declercq, J. P. (2008) The Crystal Structure of the C45S Mutant of Annelid *Arenicola marina* Peroxiredoxin 6 Supports Its Assignment to the Mechanistically Typical 2-Cys Subfamily without Any Formation of Toroid-Shaped Decamers. *Protein Sci. 17*, 700−710.
(48) Hall, A., Sankaran, B., Poole, L. B., and Karplus, P. A. (2009) Structural Changes Common to Catalysis in the Tpx Peroxiredoxin Subfamily. *J. Mol. Biol. 393*, 867−881.
(49) Stehr, M., Hecht, H. J., Jäger, T., Flohé, L., and Singh, M. (2006) Structure of the Inactive Variant C60S of *Mycobacterium tuberculosis* Thiol Peroxidase. *Acta Crystallogr., Sect. D: Biol. Crystallogr. 62*, 563−567.
(50) Choi, J., et al. (2005) Crystal Structure of the C107S/C112S Mutant of Yeast Nuclear 2-Cys Peroxiredoxin. *Proteins: Struct., Funct., Bioinf. 61*, 1146−1149.
(51) D'Ambrosio, K., Limauro, D., Pedone, E., Galdi, I., Pedone, C., Bartolucci, S., and De Simone, G. (2009) Insights into the Catalytic Mechanism of the Bcp Family: Functional and Structural Analysis of Bcp1 from *Sulfolobus solfataricus*. *Proteins: Struct., Funct., Bioinf. 76*, 995−1006.
(52) Limauro, D., D'Ambrosio, K., Langella, E., De Simone, G., Galdi, L., Pedone, C., Pedone, E., and Bartolucci, S. (2010) Exploring the Catalytic Mechanism of the First Dimeric Bcp: Functional, Structural and Docking Analyses of Bcp4 from *Sulfolobus solfataricus*. *Biochimie 92*, 1435−1444.
(53) Liao, S. J., Yang, C.-Y., Chin, K. H., Wang, A. H. J., and Chou, S. H. (2009) Insights into the Alkyl Peroxide Reduction Pathway of *Xanthomonas campestris* Bacterioferritin Comigratory Protein from the Trapped Intermediate−Ligand Complex Structures. *J. Mol. Biol. 390*, 951−966.
(54) Melchers, J., Diechtierow, M., Feher, K., Sinning, I., Tews, I., Krauth-Siegel, R. L., and Muhle-Goll, C. (2008) Structural Basis for a Distinct Catalytic Mechanism in *Trypanosoma brucei* Tryparedoxin Peroxidase. *J. Biol. Chem. 283*, 30401−30411.
(55) Muhle-Goll, C., Füller, F., Ulrich, A. S., and Krauth-Siegel, R. L. (2010) The Conserved Cys76 Plays a Crucial Role for the Conformation of Reduced Glutathione Peroxidase-Type Tryparedoxin Peroxidase. *FEBS Lett. 584*, 1027−1032.
(56) Nakamura, T., Kado, Y., Yamaquchi, T., Matsumara, H., Ishikawa, K., and Inoue, T. (2010) Crystal Structure of Peroxiredoxin from *Aeropyrum pernix* K1 Complexed with its Substrate, Hydrogen Peroxide. *J. Biochem. 147*, 109−115.
(57) Zhou, P., Tian, F., Lv, F., and Shang, Z. (2009) Geometric Characteristics of Hydrogen Bonds Involving Sulfur Atoms in Proteins. *Proteins: Struct., Funct., Bioinf. 76*, 151−163.
(58) Platts, J. A., Howard, S. T., and Bracke, B. R. F. (1996) Directionality of Hydrogen Bonds to Sulfur and Oxygen. *J. Am. Chem. Soc. 118*, 2726−2733.
(59) Baker, E. N., and Hubbard, R. E. (1984) Hydrogen Bonding in Globular Proteins. *Prog. Biophys. Mol. Biol. 44*, 97−179.
(60) Nirudodhi, S., Parsonage, D., Karplus, P. A., Poole, L. B., and Maier, C. S. (2011) Conformational Studies of the Robust 2-Cys Peroxiredoxin *Salmonella typhimurium* AhpC by Solution Phase Hydrogen/Deuterium (H/D) Exchange Monitored by Electrospray Ionization Mass Spectrometry. *Int. J. Mass Spectr. 302*, 93−100.
(61) González-Mondragón, E., Zubillaga, R. A., Saavedra, E., Chanez-Cardenas, M. E., Perez-Montfort, R., and Hernandez-Arana, A. (2004) Conserved Cysteine 126 in Triosephosphate Isomerase Is Required Not for Enzymatic Activity but for Proper Folding and Stability. *Biochemistry 43*, 3255−3263.
(62) Sayed, A. A., and Williams, D. L. (2004) Biochemical Characterization of 2-Cys Peroxiredoxins from *Schistosoma mansoni*. *J. Biol. Chem. 279*, 26159−26166.
(63) Koo, K. H., et al. (2002) Regulation of Thioredoxin Peroxidase Activity by C-terminal Truncation. *Arch. Biochem. Biophys. 397*, 312−318.
(64) Wang, F., et al. (2013) Targeted Inhibition of Mutant IDH2 in Leukemia Cells Induces Cellular Differentiation. *Science 340*, 622−626.
(65) Rhee, S. G., Jeong, W., Chang, T. S., and Woo, H. A. (2007) Sulfiredoxin, the Cysteine Sulfinic Acid Reductase Specific to 2-Cys Peroxiredoxin: Its Discovery, Mechanism of Action, And Biological Significance. *Kidney Int. 72*, S3−S8.

(66) Davis, I. W., Murray, L. W., Richardson, J. S., and Richardson, D. C. (2004) MOLPROBITY: Structure Validation and All-Atom Contact Analysis for Nucleic Acids and Their Complexes. *Nucleic Acids Res. 32*, W615−W619.
(67) Harding, M. M., Nowicki, M. W., and Walkinshaw, M. D. (2010) Metals in Protein Structures: A Review of Their Principal Features. *Crystallogr. Rev. 16*, 247−302.
(68) Vaguine, A. A., Richelle, J., and Wodak, S. J. (1999) SFCHECK: a Unified Set of Procedures for Evaluating the Quality of Macromolecular Structure-Factor Data and Their Agreement with the Atomic Model. *Acta Crystallogr., Sect. D: Biol. Crystallogr. 55*, 191−205.